Canadian Geotechnical Journal

Research Article

Novel particle reconstruction and tracking algorithms to reveal 3D micromechanical behaviors of coral sands

Ruidong LI[a], **Zhen-Yu Yin**[a,b], **Shaoheng He**[a], **and Mengmeng Wu**[a]

[a]Department of Civil and Environmental Engineering, The Hong Kong Polytechnic University, Hong Kong, China; [b]Research Centre for Nature-based Urban Infrastructure Solutions, The Hong Kong Polytechnic University, Hong Kong, China

Corresponding author: **Zhen-Yu Yin** (email: zhenyu.yin@polyu.edu.hk)

Abstract

The micromechanical behaviors of coral sands remain poorly understood, primarily due to the inherent complexity of their highly irregular particle shapes, which pose significant difficulties for accurate three-dimensional (3D) particle reconstruction and tracking using X-ray tomography (μCT). To address these challenges, this study proposes a novel framework that integrates large vision models and discrete label optimization for efficient and accurate 3D particle reconstruction with optimal transport for robust particle tracking. This framework effectively resolves tracking both particle breakage and internal voids in coral sands, as validated by in situ mini-triaxial μCT tests. Compared with the state-of-the-art method, the proposed approach achieves comparable reconstruction accuracy (90%) while reducing computational time by 50%. For particle tracking, accuracy between adjacent μCT scans (corresponding to axial strain increments of 2.5%, 5%, and 10%) reached 95%, 86%, and 71%, respectively. Micromechanical analysis of coral sands further reveals that heterogeneous local shear deformation develops as axial strain increases, forming an X-shaped shear band. Significant fabric anisotropy emerges after peak stress, with preferred orientations aligning with the shear band. Moreover, particle breakage was observed to occur primarily during the strain-softening stage. Splitting induced by stress concentration was the predominant failure mode.

Key words: X-ray tomography, coral sand, microstructure, particle breakage, anisotropy

Résumé

Les comportements micromécaniques des sables coralliens restent mal compris, principalement en raison de la complexité inhérente à leurs formes de particules très irrégulières, qui posent des difficultés importantes pour la reconstruction et le suivi précis des particules en trois dimensions (3D) à l'aide de la tomographie à rayons X (μCT). Pour relever ces défis, cette étude propose un cadre novateur qui intègre les grands modèles de vision (LVM) et l'optimisation de labels discrets (DLO) pour une reconstruction efficace et précise des particules en 3D avec un transport optimal (OT) pour un suivi robuste des particules. Ce cadre résout efficacement le suivi des ruptures de particules et des vides internes dans les sables coralliens, comme validé par des tests in-situ mini-triaxiaux μCT. Par rapport à la méthode de pointe (SOTA), l'approche proposée atteint une précision de reconstruction comparable (90 %) tout en réduisant le temps de calcul de 50 %. Pour le suivi des particules, la précision entre les scans μCT adjacents (correspondant à des incréments de déformation axiale de 2,5 %, 5 % et 10 %) a atteint 95 %, 86 % et 71 %, respectivement. L'analyse micromécanique des sables coralliens révèle en outre que des déformations locales de cisaillement hétérogènes se développent à mesure que la déformation axiale augmente, formant une bande de cisaillement en forme de X. Une anisotropie de tissu significative apparaît après le pic de contrainte, avec des orientations préférentielles s'alignant sur la bande de cisaillement. En outre, on a observé que la rupture des particules se produisait principalement au cours de la phase de ramollissement sous contrainte. Le fractionnement induit par la concentration des contraintes est le mode de défaillance prédominant.

Mots-clés : tomographie à rayons X, sable corallien, microstructure, rupture des particules, anisotropie

Introduction

Coral sands are widely distributed across tropical and subtropical continental shelves, including hydrocarbon-rich regions such as the South China Sea. Geotechnical interest in these sediments has increased significantly in recent decades due to recurrent foundation problems in offshore structures (Airey 1993; Donohue et al. 2009; He et al. 2020; Fan et al. 2021; Zeng and Liu 2023*a*). The engineering behavior of coral sands differs fundamentally from that of non-carbonate soils, exhibiting high compressibility due to particle weakness, crushability, and intricate morphology (Yasufuku and Hyde 1995; Dijkstra et al. 2013; Zeng and Liu 2023*b*; Shen et al.

2024). Crucially, their macro-mechanical responses are significantly governed by micro-mechanical processes (He et al. 2024*b*). For instance, coral sands exhibit an extremely loose fabric with a high void ratio when subjected to loading (Kong and Fonseca 2019). The unlocking mechanism posits that particle breakage and rearrangement (e.g., sliding and rotation) degrade fabric stability and reduce stiffness (Mesri and Vardhanabhuti 2009; Zeng and Liu 2023*c*, 2025), triggering transient contact loss and eventual fabric collapse. However, the underlying micromechanisms of coral sands remain inadequately characterized. Elucidating these particle-scale characteristics is essential for optimizing geotechnical designs in coral sand environments.

In situ triaxial tests enhanced by X-ray micro-tomography (μCT) technique have emerged as a powerful methodology for analyzing micromechanical behaviors of sands through non-destructive three-dimensional (3D) imaging of internal structures (Andò et al. 2012; Alikarami et al. 2015; Imseeh et al. 2018; Amirrahmat et al. 2019; Wiebicke et al. 2021; Elnur and Alshibli 2023; Pinzón et al. 2023). For example, Desrues et al. (1996) achieved shear band visualization in Hostun RF sand using μCT, demonstrating how localization patterns vary with test conditions. For particle kinematics, Watanabe et al. (2012) developed a μCT-based technique quantifying displacements of Yamazuna sand particles during triaxial loading. Regarding particle breakage, Wu and Wang (2023) identified crushing mechanisms in quartz and calcite sands, noting preferential fracturing of angular particles. Most recently, Hu et al. (2025) performed μCT triaxial tests on 5–10 mm coral sands under various confining pressures using a horizontal apparatus with medical CT equipment. However, in this configuration, the misalignment between gravity (vertical) and maximum compression (horizontal) may limit extrapolation of shear band localization and fabric evolution to field conditions.

Critically, studies utilizing μCT-based triaxial testing on 1–2 mm coral sands are lacking, primarily due to unresolved challenges in particle reconstruction and tracking from 3D image data. Particle reconstruction refers to identifying individual particles from volumetric images. The conventional approach employs a modified watershed algorithm that separates contacting particles by detecting watershed lines between local minima in inverted Euclidean distance transform maps (Kong and Fonseca 2018). However, this method demands specialized expertise for local minima identification and substantial manual correction for coral sands, hindering practical implementation, especially for coral sands. Over the past 2 years, large vision models (LVMs) have gained prominence in solving complex challenges, such as medical image segmentation (Zhang et al. 2024), damage detection (Ge et al. 2024), and remote sensing (Osco et al. 2023). Li et al. (2025*a*) pioneered an LVM-optimal transport (OT) framework for reconstructing 3D particles from μCT images. In this approach, LVMs convert 2D μCT slices into segmented images while OT integrates these into one complete 3D image for particle reconstruction. Subsequently, Li et al. (2025*b*) streamlined the LVM implementation and introduced an advanced OT scheme, achieving accelerated processing while maintaining reconstruction accuracy. Despite achieving state-of-the-art (SOTA) accuracy, these LVM-OT-based methods remain computationally intensive because they require processing slices along three orthogonal axes.

Table 1. Physical characteristics of coral sands.

Dataset	Value
Specific gravity (G_s)	2.75
Maximum void ratio (e_{max})	1.347
Minimum void ratio (e_{min})	0.91
Medium particle size (d_{50})	1.403
Coefficient of uniformity (C_u)	1.514
Coefficient of curvature (C_c)	1.089
Relative density (D_r)	80%

Particle tracking presents additional complexities, requiring similarity metrics such as volumetric differentials (Andò et al. 2012), shape invariants (Zhou et al. 2018), and point cloud registration (Wu and Wang 2019) to correlate particles across deformation states. While Wu et al. (2023) proposed a deep-learning solution, it was only validated on isolated artificially marked coral sand particles. None of these methods has been validated for tracking coral sands during shearing. Notably, OT algorithms have succeeded in cell tracking (Liu et al. 2023) and shape matching (Shen et al. 2021), yet their potential for particle tracking remains unexplored. Consequently, accurate reconstruction and tracking of coral sands under triaxial shear with μCT represents a fundamental research gap requiring resolution to advance micromechanical understanding.

To address these limitations, this study proposes a novel framework integrating LVMs and discrete label optimization (DLO) for 3D particle reconstruction and OT for 3D particle tracking. The approach is validated through the in situ μCT drained triaxial compression test on coral sands. Qualitative and quantitative benchmarks demonstrate significant improvements in computational efficiency and accuracy over the SOTA method. Furthermore, leveraging these high-fidelity results, we provide the first comprehensive μCT-based micromechanics analysis of coral sand during in situ triaxial compression, which precisely captures the evolution of particle kinematics, contact fabric, and breakage patterns.

Test materials and experiment

Test materials and set-ups

The tested coral sands were sourced from the Xisha Islands in the South China Sea (He et al. 2020, 2024*a*). The key physical characteristics of the tested sands, determined according to ASTM C136-06 (ASTM 2006), ASTM C127-15 (ASTM 2014), and ASTM D2487-17 (ASTM 2017) standards, are summarized in Table 1. Figure 1*a* illustrates the particle size distribution of the coral sand, alongside images depicting its highly irregular particle morphology, characterized by angular shapes, rough surface textures, and abundant intra-particle voids. Figure 1*b* depicts the classification of particle shapes into ten categories based on the Sneed and Folk (1958) classification system. The majority of the coral sand particles

Fig. 1. Materials and apparatus: (*a*) particle size distribution and typical coral sand particles; (*b*) particle shape classification; and (*c*) detector and mini-triaxial apparatus. CSS, coral sand specimen.

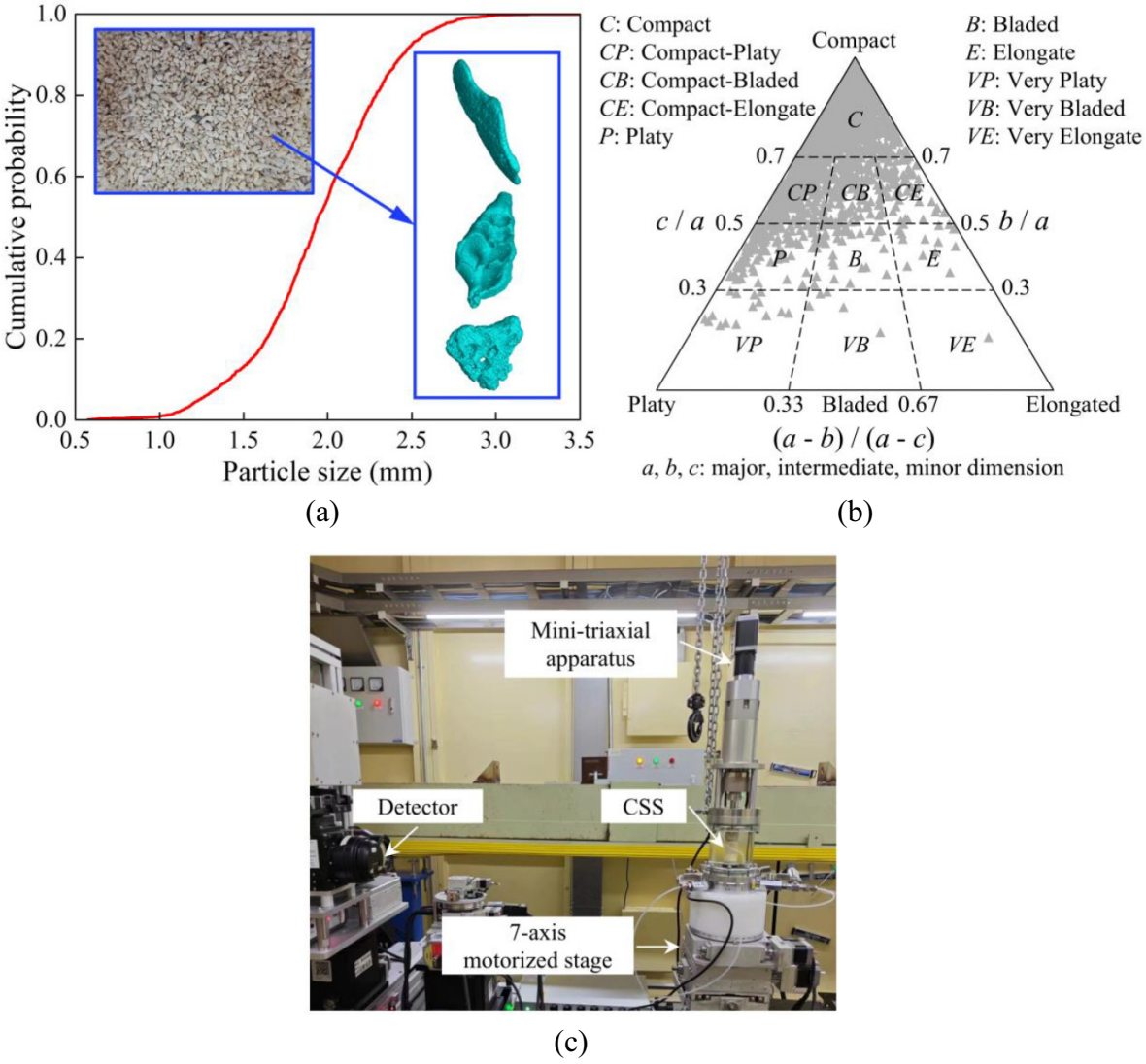

analyzed were classified as “Compact” or “Sub-compact” types, with only a minor portion categorized as “Platy”, “Bladed”, or “Elongated”. In this study, in situ triaxial tests on the coral sands were conducted using a mini-triaxial apparatus (KTL Instruments Ltd., China) at the BL13HB X-ray Imaging and Biomedical Application Beamline (Ji et al. 2023) of the Shanghai Synchrotron Radiation Facility (SSRF), as shown in Fig. 1*c*. This mini-triaxial apparatus primarily comprises a loading system, a confining pressure supply system, and a data acquisition system (more detailed descriptions can be found in Wu and Wang (2023)). During testing, the mini-triaxial apparatus was positioned on a high-precision 7-axis motorized stage located between the X-ray source and detector, with the coral sand specimen (CSS) contained within the triaxial cell.

Specimen preparation and test procedures

Figure 2 illustrates the preparation procedure for the CSS (20 mm diameter × 40 mm height) using the dry deposition method in accordance with ASTM (2015). Initially, dry coral sands were slowly poured into the mold in four layers using a funnel, with each layer subsequently compacted by manual tamping with a hammer. A suction pressure of 20 kPa was subsequently applied to facilitate mold disassembly. Afterwards, the pressure chamber and loading apparatus were installed. Saturation of the CSS was achieved through the sequential application of the carbon dioxide (CO_2) saturation and the back pressure saturation (He et al. 2023). The saturation process was considered complete when the pore-pressure coefficient *B* exceeded 0.95 (Skempton 1954); otherwise, the back-pressure saturation stage was repeated. Finally, the fully saturated CSS was consolidated and sheared under drained conditions at an axial strain rate of 0.5% / min (Zhang et al. 2023).

In this study, three mini-triaxial tests were conducted under confining pressures of 50, 100, and 150 kPa. This stress range was selected to effectively demonstrate the proposed particle reconstruction and tracking technique and

Fig. 2. Specimen preparation.

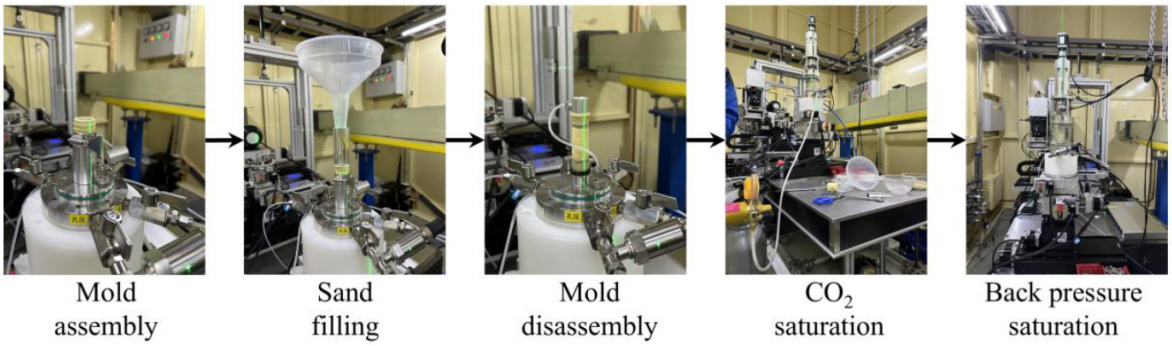

to reveal distinct micromechanical trends under moderate confinement. The successful application of this methodology under these conditions will pave the way for its future application at higher stress levels. Due to the substantial resources required for high-resolution in situ CT scanning and the limited availability of scanning time, the CSS under 100 kPa confining pressure was chosen for scanning at five axial strain levels: 0%, 2.5%, 5%, 10%, and 20%. This intermediate stress level offers an optimal balance for initiating observable particle breakage without the limited breakage occurring at 50 kPa or the potential complications arising from excessive fragmentation at 150 kPa.

To overcome the limited field of view of the detector, a full 3D image of the CSS was acquired by stitching 20 overlapping localized scans. Each localized scan, requiring approximately 2 min, involved rotating the specimen by 180° (clockwise or counterclockwise) and translating the specimen stage vertically by 2 mm. A vertical overlap of approximately 1.61 mm between consecutive scan positions was maintained to facilitate accurate image stitching. Importantly, axial shearing was paused during each scan while the confining pressure was held constant. The X-ray source energy was optimized for scanning efficiency at 35 keV. Raw μCT projections were reconstructed into image slices using the PITRE software (Chen et al. 2012). Representative orthogonal μCT slices (image resolution = 9 μm/voxel) and the corresponding 3D rendered view of the CSS are presented in Figs. 3*a* and 3*b*, respectively.

Macroscopic mechanical behaviors

The definitions of the axial strain ε_a, deviatoric stress q, and volumetric strain ε_v are presented as follows:

$$\varepsilon_a = \frac{H_0 - H}{H_0} \quad (1)$$

$$q = \sigma_a - \sigma_c \quad (2)$$

$$\varepsilon_v = \frac{V - V_0}{V_0} \quad (3)$$

where H_0 and H are the initial height and the current height of CSS, respectively; σ_a and σ_c represent the axial effective principal stress and confining pressure, respectively; V_0 and V denote the initial volume and current volume, respectively.

Figure 4 illustrates the evolution of deviatoric stress q and volumetric strain ε_v versus axial strain ε_a under three confining pressures. All specimens exhibit similar macromechanical behavior trends: deviatoric stress increases (hardening) to a peak value and subsequently decreases (softening) with increasing axial strain, while volumetric strain transitions from contraction to dilation. Increasing confining pressure increases both the initial shear modulus and peak deviatoric stress but reduces the degree of post-peak softening and dilatancy. Furthermore, the axial strains at both peak stress and the phase transformation state (where volumetric strain changes from contraction to dilation) increase with higher confining pressure. These trends are consistent with the findings of He et al. (2021).

Novel method for image processing and analysis

LVM-based 3D particle reconstruction

The most widely used method for reconstructing CSS from μCT images is the modified watershed algorithm (Kong and Fonseca 2018). While computationally efficient, this approach exhibits limitations in reconstruction accuracy. In contrast, the particle reconstruction method proposed by Li et al. (2025*b*) achieves superior accuracy through integration of the large vision model (LVM) and optimal transport (OT) theory. However, this method requires computationally intensive 2D segmentation of all slices along three orthogonal axes, resulting in high computational costs. To address these problems, a novel two-step method integrating LVM and DLO for accurate and efficient CSS reconstruction is proposed (Fig. 5).

The first step is to convert all μCT slices along the arbitrary one axis (e.g., *x*-axis) and N uniformly spaced slices along another axis (e.g., $N = 80$, corresponding to the 1st, 21st, 41st, …, and 1600th slices) into 2D segmentations using the LVM. In this study, a SOTA LVM, the Segment Anything Model 2 (SAM 2) with a 40 × 40 grid of point prompts, is used for demonstration (Ravi et al. 2024). In LVM, each μCT slice is encoded into a low-dimensional latent representation by the

Fig. 3. X-ray micro-tomography (μCT) images: (*a*) orthogonal slices; and (*b*) 3D view.

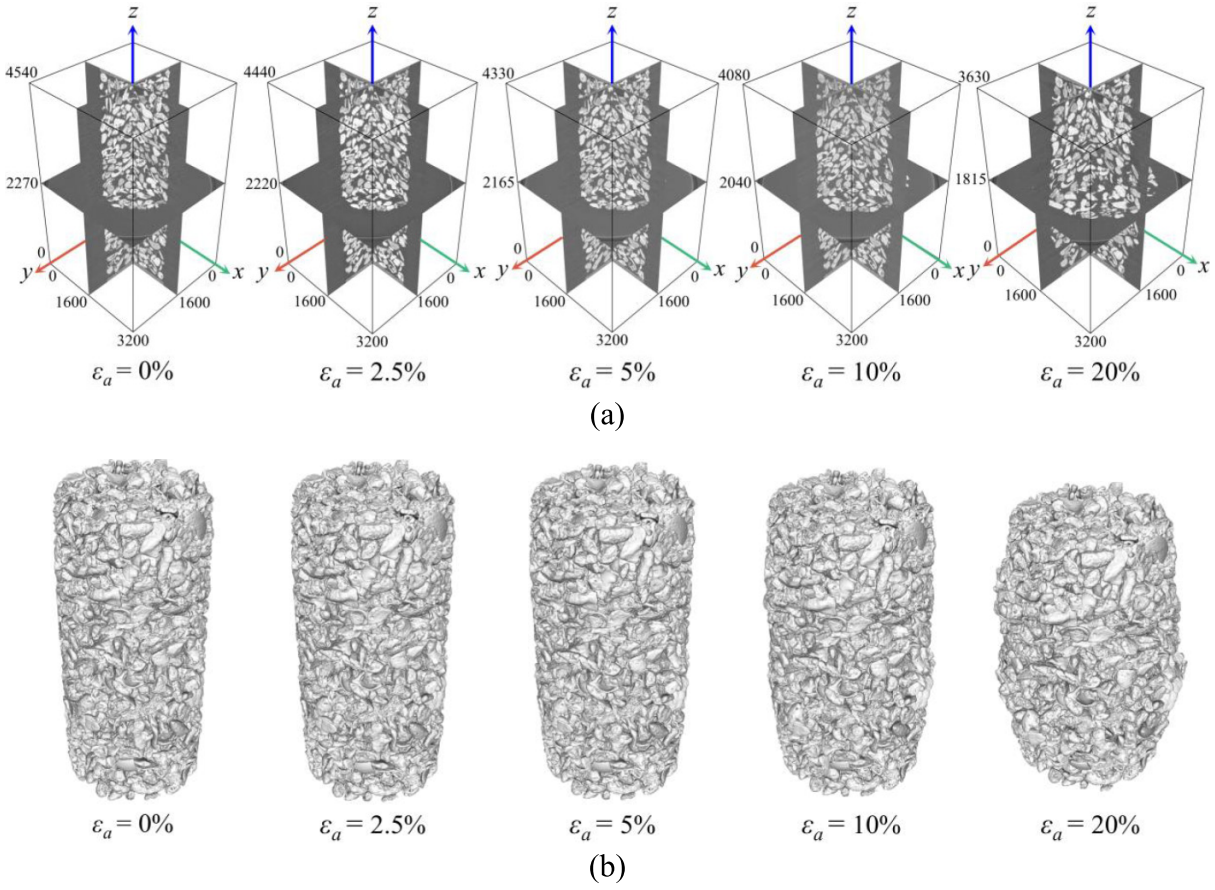

Fig. 4. Evolutions of deviatoric stress q and volumetric strain ε_v versus axial strain ε_a.

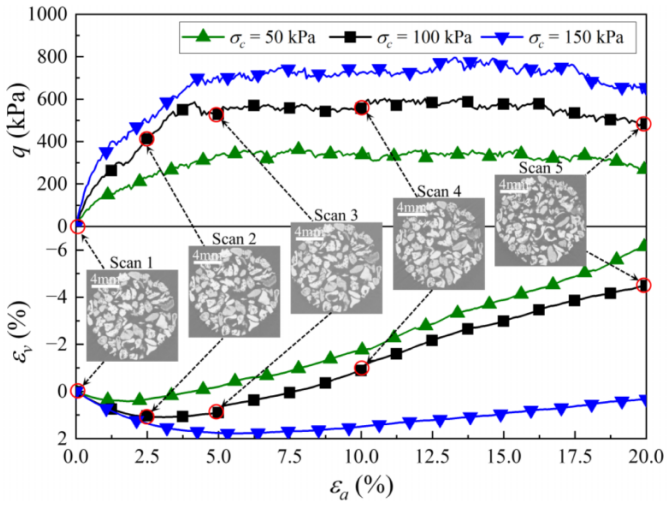

image encoder, while point prompts generate corresponding embedding vectors via the prompt encoder. These complementary embeddings are subsequently fused within the mask decoder to output scored masks denoting particles. Only masks exceeding a confidence score threshold (≥0.95) were retained and assigned unique labels. Finally, Otsu's thresholding algorithm (Otsu 1979) was applied to refine morphological characteristics, such as intraparticle voids, and to remove noise-induced artifacts. Thus, the collection of validated labels within each slice forms a 2D segmentation. This study illustrates the approach using slices along the *x*- and *y*-axes. Moreover, the sets of 2D segmentations along the *x*- and *y*-axes are denoted as $\boldsymbol{X}$ and $\boldsymbol{Y}$, respectively, both maintaining the original dimensions of μCT images. For the non-sampled slices along the *y*-axis, the corresponding entries in $\boldsymbol{Y}$ are filled with zero matrices.

The second step is to reconstruct 3D particles based on $\boldsymbol{X}$ and $\boldsymbol{Y}$ using the DLO scheme. In DLO, the nonzero segmentations along the *y*-axis in $\boldsymbol{Y}$ are extracted and denoted as $\boldsymbol{Y}_Y$, and corresponding *y*-axis-aligned segmentations in $\boldsymbol{X}$ are designated as $\boldsymbol{X}_Y$

$$\boldsymbol{X}_Y = \left\{\boldsymbol{X}_Y^i\right\}_{i=1}^N,\ \boldsymbol{Y}_Y = \left\{\boldsymbol{Y}_Y^i\right\}_{i=1}^N \tag{4}$$

where $\boldsymbol{X}_Y^i$ and $\boldsymbol{Y}_Y^i$ denote the *i*th slice in $\boldsymbol{X}_Y$ and $\boldsymbol{Y}_Y$, respectively. Notably, for each nonzero label l in $\boldsymbol{Y}_Y^i$, the labels at the identical positions in $\boldsymbol{X}_Y^i$ are assumed to represent the same particle p. Consequently, the voxel positions of p in the 3D segmentation $\boldsymbol{S}$ are denoted as $\boldsymbol{\Omega}$ and can be calculated based on $\boldsymbol{X}$ as follows:

$$\Omega = \bigcup_{k\in\xi}\left\{(x_k, y, z)|\boldsymbol{X}(y, z) = k \neq 0\right\} \tag{5}$$

$$\xi = \left\{\boldsymbol{X}(y, z)|\boldsymbol{Y}_Y^i(x, z) = l\right\} \tag{6}$$

Fig. 5. 3D particle reconstruction by LVM-DLO. LVM, large vision model; DLO, discrete label optimization

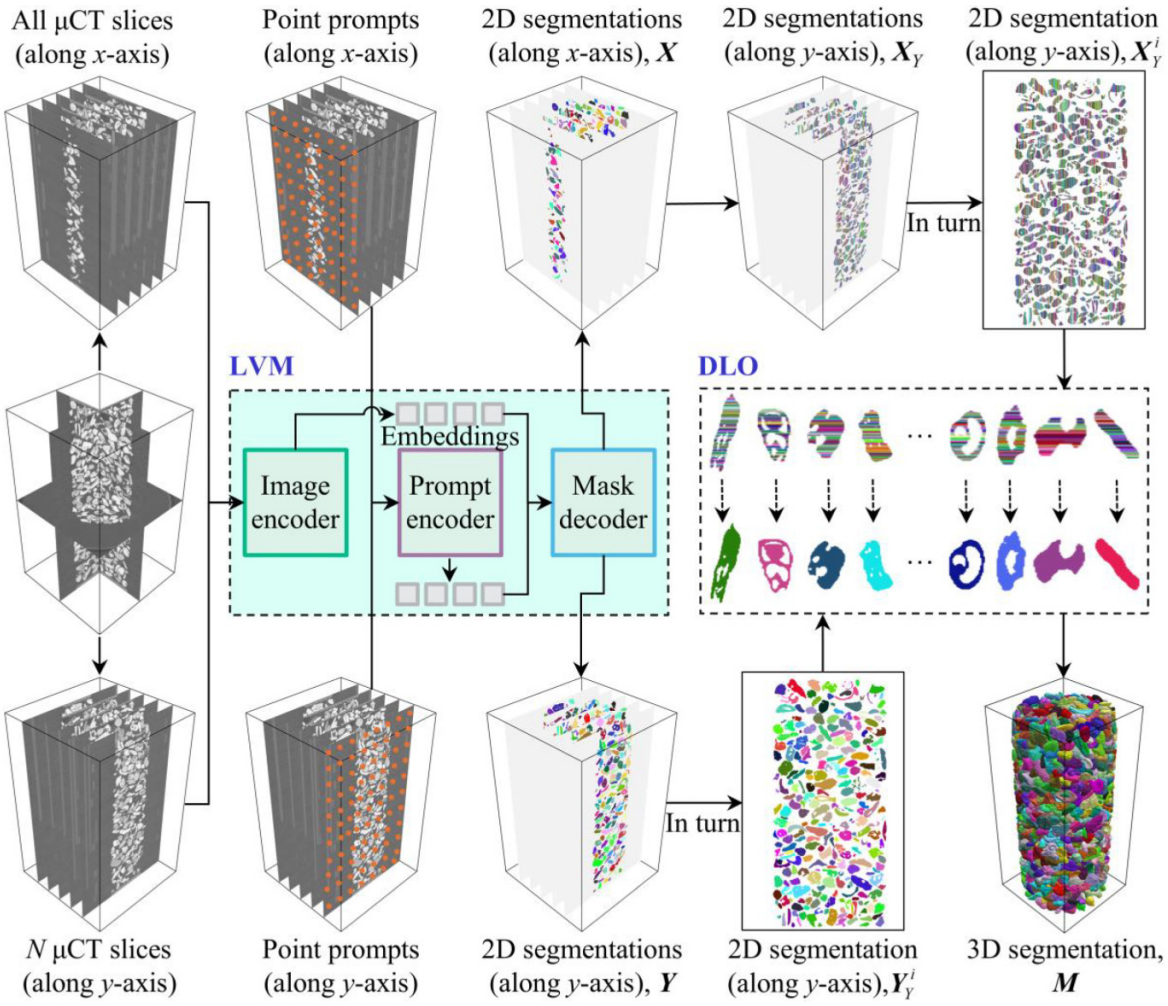

where x_k is the kth slice along the x-axis; x, y, and z denote the coordinates along the x-, y-, and z-axes, respectively; ξ represents the set of slice indices along the x-axis for p in $\boldsymbol{X}$. To label these voxels in $\boldsymbol{S}$, a labeling scheme is proposed

$$L_T = \begin{cases} \text{mode}\left(\{G(v) \in v \in \Omega, G(v) \neq 0\}\right) & \text{if } \exists \\ \max(M) + 1 & \text{otherwise} \end{cases} \tag{7}$$

where L_T is the new label value for $\boldsymbol{\Omega}$ in $\boldsymbol{M}$; mode(·) and max(·) represent mode and maximum function, respectively; and G(·) corresponds to the label acquisition function. This procedure is iteratively applied to all labels within each slice in $\boldsymbol{Y}_Y^i$. Therefore, the discrete 2D segmentations along the x-axis (in $\boldsymbol{X}$) can be integrated or correlated using the high-fidelity particle information derived from the sampled slices along the y-axis (in $\boldsymbol{Y}$). Finally, 3D coral sand particles can be reconstructed in the form of point clouds by the marching cube algorithm (Lorensen and Cline 1987) from $\boldsymbol{M}$. Crucially, the number of sampled slices N along the auxiliary axis (e.g., y-axis) significantly impacts the completeness and accuracy of the reconstructed 3D particles. Insufficient sampling (N too small, e.g., 20) may yield incomplete particle reconstructions due to inadequate morphological coverage. Importantly, the primary advantage of this method is its elimination of the need for redundant 2D segmentations along three orthogonal axes and avoidance of 2D-to-3D mapping using OT. By leveraging DLO, the approach processes slices along only one axis via the LVM, theoretically achieving approximately 2× faster processing speed compared to the LVM-OT method that requires segmentation along three axes. Notably, the robust identification capability and versatility of LVM facilitate the reconstruction of diverse granular materials directly from μCT slices (Li et al. 2025*b*).

OT-based 3D particle tracking

Particle tracking is essential for analyzing particle kinematics and breakage. However, to the best of the author's knowledge, there are currently no validated algorithms or case studies for tracking packed coral sands under shear. To fill this gap, a three-step generic approach based on OT was proposed.

The first step is to identify candidate particles in the adjacent previous scan for the target particle in the current scan based on reconstruction results (Fig. 6). For instance, for a target particle p at $\varepsilon_a = 2.5\%$, its candidate particles for tracking at $\varepsilon_a = 0\%$ are defined as those located within or intersecting the bounding box for tracking (BBT) centred at the centroid of p. The dimension $\boldsymbol{D}_c$ of BBT is calculated by

Fig. 6. Identification of candidate particles.

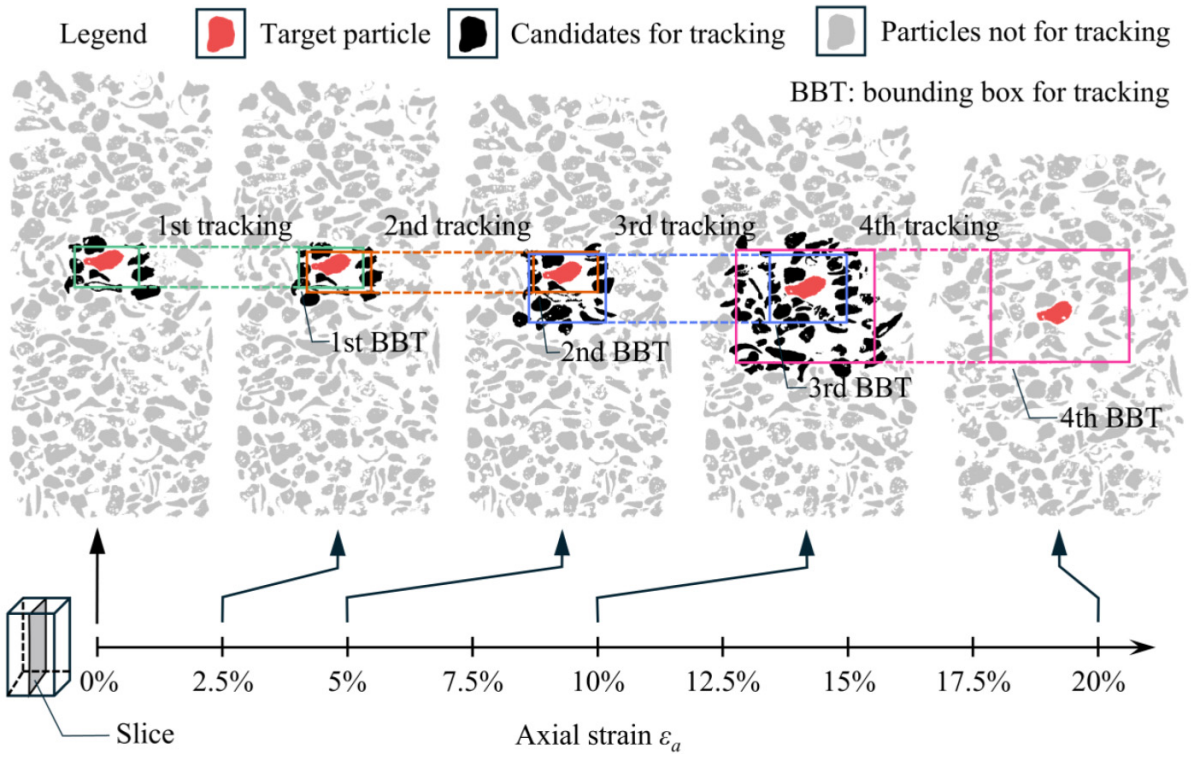

$$\boldsymbol{D}_c = \omega \boldsymbol{D}_t \tag{8}$$

$$\omega = \max\left(1, \frac{I_s}{3}\right) \tag{9}$$

where $\boldsymbol{D}_t$ is the dimension of the bounding box for the source particle p; ω denotes the scaling factor; I_s represents scan intervals (e.g., equal to 2.5 for tracking between scans at $\varepsilon_a = 0\%$ and $\varepsilon_a = 2.5\%$). Although full pairwise particle matching between adjacent scans (Wu and Wang 2023), our method significantly narrows the search scope for particle matching, theoretically enhancing computational efficiency.

The second step is to determine the optimal matchings between particles in adjacent scans by OT. For adjacent scans K_s (M particles) and K_{s+1} (N particles), the OT-based tracking formulation is expressed as

$$\mathrm{OT}(K_s, K_{s+1}) = \min_{\alpha \in \mathbb{R}_{\geq 0}^{N \times M}} \sum_{i=1}^{N} \sum_{j=1}^{M} \alpha_{i,j} \beta_{i,j} \tag{10}$$

where $\alpha_{i,j}$ denotes the matching probability between particles i and j, which was set to be identical for all particle pairs in this study; and $\beta_{i,j}$ represents the cost function and is defined as follows:

$$\beta_{i,j} = (1 - e_{i,j})^2 \frac{\|V_i - V_j\| \, \|S_i - S_j\|}{V_i S_i} c_0 \tag{11}$$

where V_i and V_j are the volumes of particles i and j, respectively; S_i and S_j denote the surface areas of particles i and j, respectively; c_0 is the default cost, set to 10^{10}; and $e_{i,j}$ represents the registration error between particles i and j, which is calculated by the TEASER++ algorithm (Yang et al. 2021) as follows:

$$e_{i,j} = \sqrt{\frac{1}{N_{pp}} \sum_{k=1}^{N_{pp}} \left\| q_k - (\widehat{\boldsymbol{R}} p_k + \widehat{\boldsymbol{t}}) \right\|} \tag{12}$$

where N_{pp} denotes the number of point pairs between particles i and j; q_k and p_k are the kth point of particle i and j, respectively; $\widehat{\boldsymbol{R}}$ and $\widehat{\boldsymbol{t}}$ represent the estimated rotation matrix and translational vector computed by the Teaser++ algorithm, respectively. TEASER++ is a fast and certifiably robust point cloud registration algorithm that estimates the optimal rigid transformation even in the presence of extreme outlier correspondences. In this study, TEASER++ quantifies the similarity between particles in the form of point clouds. Compared to Fast Global Registration (Zhou et al. 2016) and Iterative Closest Point (Wu and Wang 2023), TEASER++ requires no prior initialization, provides theoretical guarantees of global optimality, and demonstrates superior robustness and efficiency, especially when reliable correspondences (already determined by the first step) are available. More details about the TEASER++ algorithm can be found in Yang et al. (2021). Notably, to improve computational efficiency, the cost calculation is restricted to source-candidate particle pairs as defined in eq. 11, while costs between other particle pairs are set to c_0.

The third step is to identify particle breakage and align adjacent particle tracking results. Particles that are tracked by OT but have a relative volume difference exceeding 10% are reprocessed by repeating the second step with the following

Fig. 7. Sensitivity analysis of parameter N on reconstruction accuracy.

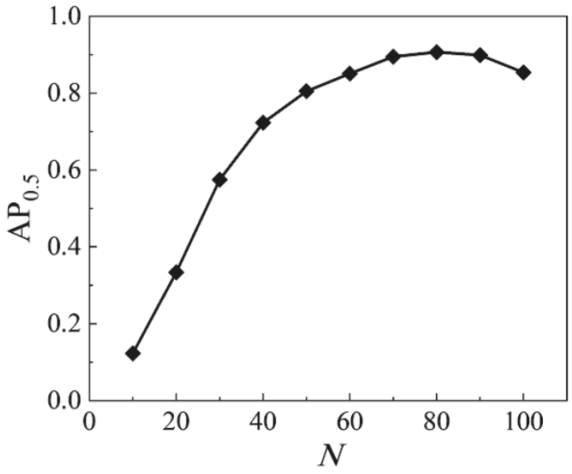

cost function

$$\beta_{i,j} = (1 - e_{i,j})c_0 \quad (13)$$

This modified cost function prioritizes particle morphology similarity while disregarding volume or area changes, significantly enhancing the accuracy of particle breakage identification. Ultimately, all adjacent tracking results are merged sequentially to enable continuous tracking from the initial to any subsequent scan. Notably, the proposed particle tracking method leverages the fundamental physical and morphological characteristics of particles, which underpins its robustness and universal applicability to arbitrary granular materials.

Validation and evaluation

In this study, the most widely employed evaluation metric in particle reconstruction, average precision (AP), is used to assess the accuracy of 3D particle reconstruction and is defined as follows (Davis and Goadrich 2006):

$$\mathrm{AP} = \frac{\mathrm{TP}}{\mathrm{TP} + \mathrm{FN} + \mathrm{FP}} \quad (14)$$

where TP is the number of correctly reconstructed particles; FP denotes the number of incorrectly reconstructed particles; and FN represents the number of unreconstructed particles. The correctly reconstructed particles are those exhibiting an Intersection over Union (IoU) greater than a specified threshold (typically 0.5 is sufficient) with their corresponding ground-truth particles (Rezatofighi et al. 2019). Moreover, $AP_{0.5}$ denotes the AP value at the IoU = 0.5 and so forth.

To assess the sensitivity of reconstruction accuracy with respect to parameter N, Fig. 7 plots the variation of $AP_{0.5}$ as N increases from 10 to 100 in increments of 10, exemplified by the CSS at 0% strain. The results indicate that reconstruction accuracy improves steadily with increasing N up to 80, a trend attributable to the integration of more information from orthogonal orientations. Beyond $N = 80$, however, a slight decline in accuracy is observed, likely resulting from the amplification of intrinsic noises or reconstruction errors. Therefore, N was set to 80 in this study to optimize the algorithmic performance. It should also be noted that the optimal N depends on the particle size distribution. Specifically, specimens with larger average particle sizes generally require higher values of N, whereas lower values are sufficient for finer-grained materials.

Figure 8 qualitatively compares representative slices of raw images with reconstructed images generated by the watershed method (Kong and Fonseca 2018), LVM-OT (Li et al. 2025*b*), and our proposed LVM-DLO method across five scans. It can be observed that the watershed method demonstrates suboptimal reconstruction performance, with pervasive errors. Conversely, both LVM-OT and the LVM-DLO approach yield substantially improved results, exhibiting only two to three reconstruction errors per slice. These qualitative observations are quantitatively corroborated in Table 2, which evaluates CSS reconstruction performance across methodologies. All three methods demonstrate consistent performance across five reconstructions, as validated by comparable AP values and computational times. The watershed method achieves only 35% $AP_{0.5}$ accuracy, declining to merely 10% at $AP_{0.9}$, substantially inferior to LVM-based approaches. Notably, both LVM-OT and LVM-DLO methods achieve similar reconstruction accuracy, with $AP_{0.5} \approx 91\%$. However, LVM-OT outperforms the LVM-DLO method under stricter metrics: at IoU thresholds of 0.75 and 0.9, it exceeds the LVM-DLO by 5% and 10%, respectively. Conversely, LVM-DLO reduces computational time by nearly 50% compared to LVM-OT. This efficiency gain stems from eliminating multi-axis 2D segmentation and replacing conventional 2D-to-3D mapping with a simpler DLO. Although the additional DLO processing prevents a full 2× speedup, LVM nevertheless maintains high accuracy while significantly enhancing computational efficiency. These results collectively demonstrate the dual advantages of our proposed LVM-DLO framework for efficient and accurate 3D particle reconstruction.

To quantify the tracking accuracy of the proposed OT-based method, two metrics (single tracking accuracy A_s and end-to-end tracking accuracy A_e) are adopted and defined as follows:

$$A_s = \frac{N_{cs}}{N_{ps}} \quad (15)$$

$$A_e = \frac{N_{cs}}{N_{is}} \quad (16)$$

where N_{ps} denotes the number of particles in the adjacent previous scan; N_{cs} is the number of correctly tracked particles in the current scan; and N_{is} represents the number of particles at the initial state (0% strain). A_s evaluates the effectiveness of the particle tracking method, while A_e measures its robustness and reliability. Note that for a particle that undergoes breakage, it is considered accurately tracked only when all resulting fragments are correctly tracked.

Figure 9 presents representative cross-sectional slices and 3D renderings of particle tracking results. Visual inspection confirms consistent color assignments across successive reconstructions, indicating accurate tracking for most particles. However, tracking errors occur at large scan intervals

Fig. 8. Qualitative evaluation of different methods in reconstructing CSS: (*a*) raw image; (*b*) watershed; (*c*) LVM-OT; and (*d*) LVM-DLO. Note that the black dashed circles denote the reconstruction errors. LVM, large vision model; OT, optimal transport; DLO, discrete label optimization.

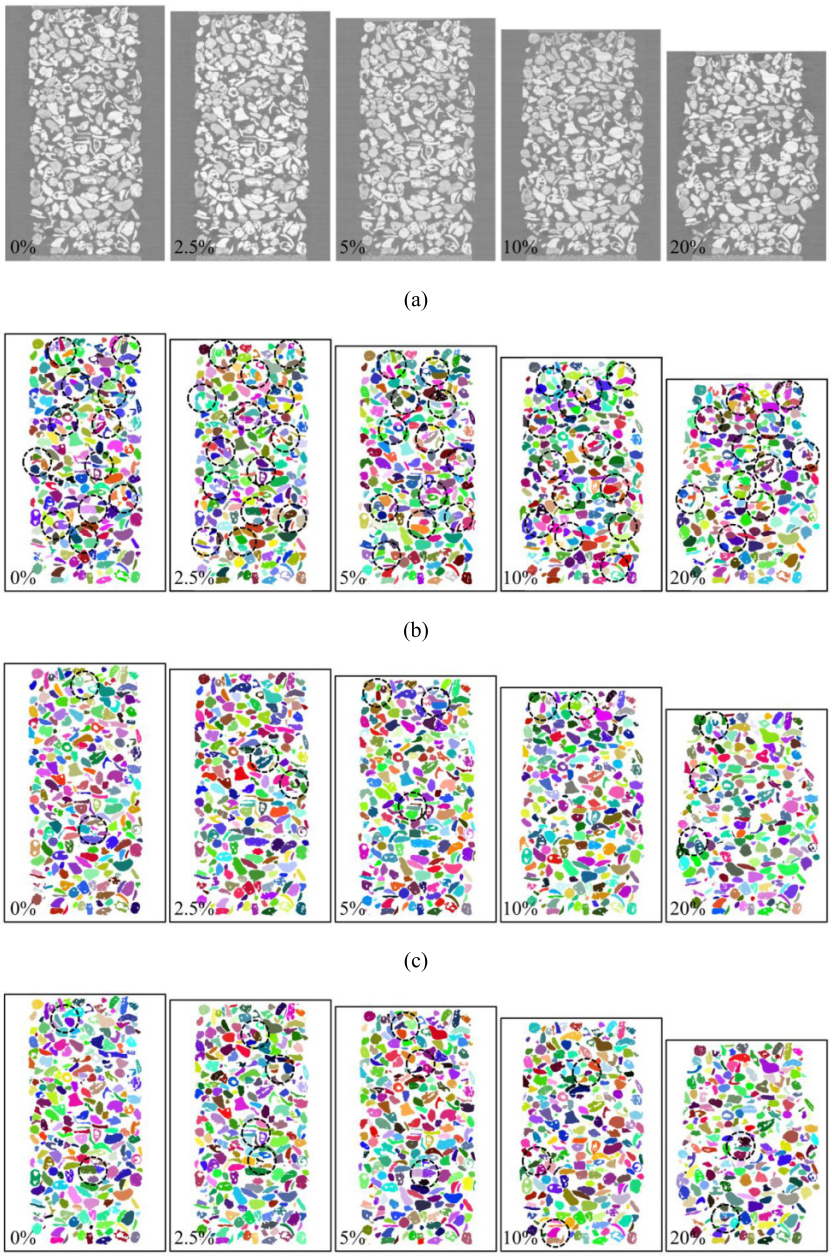

(e.g., $I_s = 10$). Crucially, our method successfully resolves particle breakage cases, as demonstrated within the black solid circle where a parent particle bifurcates into two daughter fragments at 10% strain. Table 3 illustrates the quantitative evaluation of the proposed method in tracking coral sand particles. The OT-based method achieves satisfactory performance at small scan intervals of $I_s = 2.5$, attaining nearly 95% A_s. For large scan intervals ($I_s \geq 5$), A_s remains robust at 86% and 71%, respectively, demonstrating method efficacy. End-to-end tracking accuracy exhibits strain-dependent degradation, declining from approximately 93% at 5% strain to approximately 60% at 20% strain. This degradation primarily stems from two factors: the accumulation of errors propagated from earlier tracking stages, and the failure to match particles located outside the BBT, which is caused by significant particle rearrangements at 10% strain intervals. To address this limitation and enhance matching reliability under large deformations, future work will focus on implementing an expanded BBT and developing more advanced matching criteria.

Notably, computational times of our method are relatively low: small scan intervals ($I_s = 2.5$) require only 20 min, while larger scan intervals such as $I_s = 5$ and $I_s = 10$ necessitate 60 and 120 min, respectively. This computational efficiency

Table 2. Quantitative evaluation of different methods in reconstructing CSS.

Methods	Strains (%)	$AP_{0.5}$	$AP_{0.75}$	$AP_{0.9}$	Computational time (s)
Watershed	0	0.361	0.238	0.117	754
	2.5	0.358	0.232	0.108	746
	5	0.362	0.237	0.115	752
	10	0.357	0.239	0.111	745
	20	0.356	0.228	0.113	747
LVM-OT	0	0.932	0.846	0.739	7346
	2.5	0.924	0.845	0.729	7318
	5	0.926	0.837	0.729	7375
	10	0.925	0.843	0.732	7326
	20	0.911	0.856	0.743	7361
LVM-DLO	0	0.907	0.798	0.638	3643
	2.5	0.919	0.801	0.622	3627
	5	0.905	0.794	0.635	3686
	10	0.914	0.800	0.633	3602
	20	0.915	0.803	0.624	3664

Note: CSS, coral sand specimen; LVM, large vision model; OT, optimal transport; DLO, discrete label optimization.

Fig. 9. Qualitative evaluation of the proposed method in tracking coral sand particles: (*a*) slice view; and (*b*) 3D view. Note that the black dashed circle represents the reconstruction error, while the solid circle highlights the particle breakage.

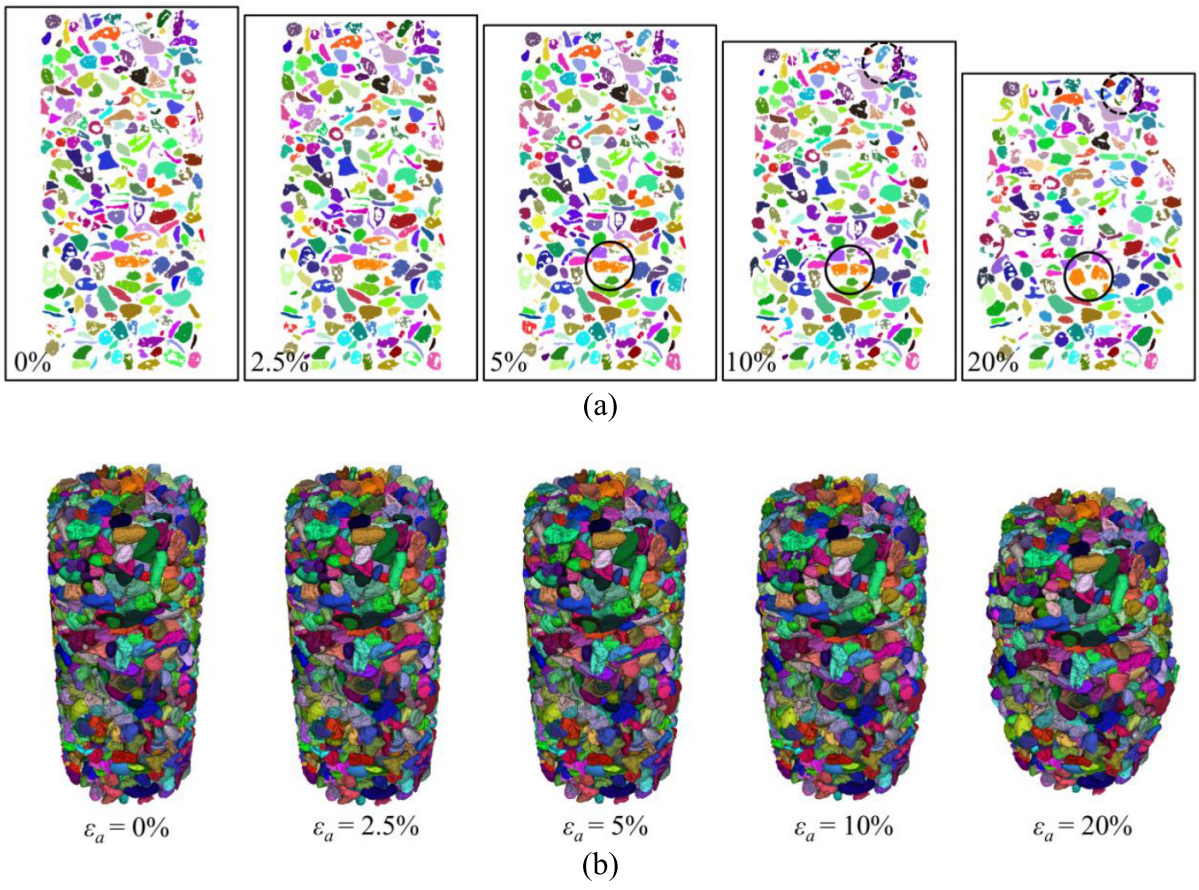

represents a significant improvement over the 5-day benchmark reported by Wu and Wang (2023) for datasets with fewer particles and simpler morphologies. Collectively, these results demonstrate that our tracking method provides both computationally efficient and metrologically robust particle tracking, enabling high-resolution analysis of particle kinematics and breakage in CSS. To ensure analytical correctness in microstructural evolution studies, all particle reconstruction and tracking results undergo rigorous manual verification and repair.

Table 3. Quantitative evaluation of the proposed method in tracking coral sand particles.

Methods	Adjacent previous strain (%)	Current strain (%)	A_s	A_e	Computational time (s)
OT-based	0	2.5	0.973	0.973	1204
	2.5	5	0.958	0.933	1270
	5	10	0.863	0.810	3564
	10	20	0.711	0.592	11640

Note: OT, optimal transport.

Fig. 10. Particle displacement and rotation during axial strain increments of: (*a*) 0%–2.5%; (*b*) 2.5%–5%; (*c*) 5%–10%; and (*d*) 10%–20%.

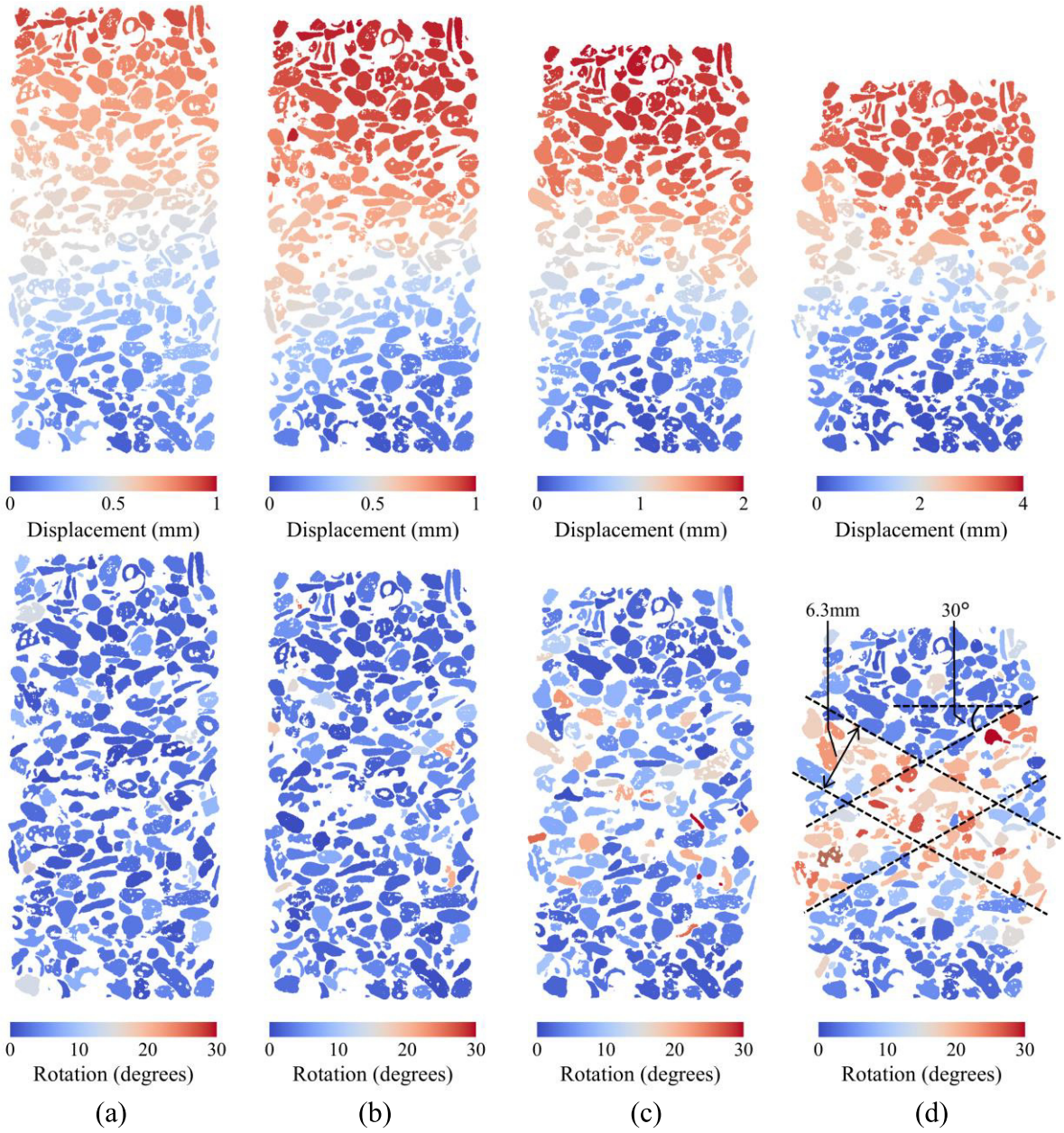

Micromechanical behaviors

Particle kinematic

Particle kinematics, including particle displacements and rotations during shearing, are fundamental to understanding the granular micromechanics of coral sands. The 3D displacement of individual particles is quantified by tracking changes in the coordinates of particle centroid between scans (Andò et al. 2012), while rotations are determined by analyzing changes in particle orientation (Cheng and Wang 2018). For

Fig. 11. Evolution of the coordination number with particle volume at different axial strains.

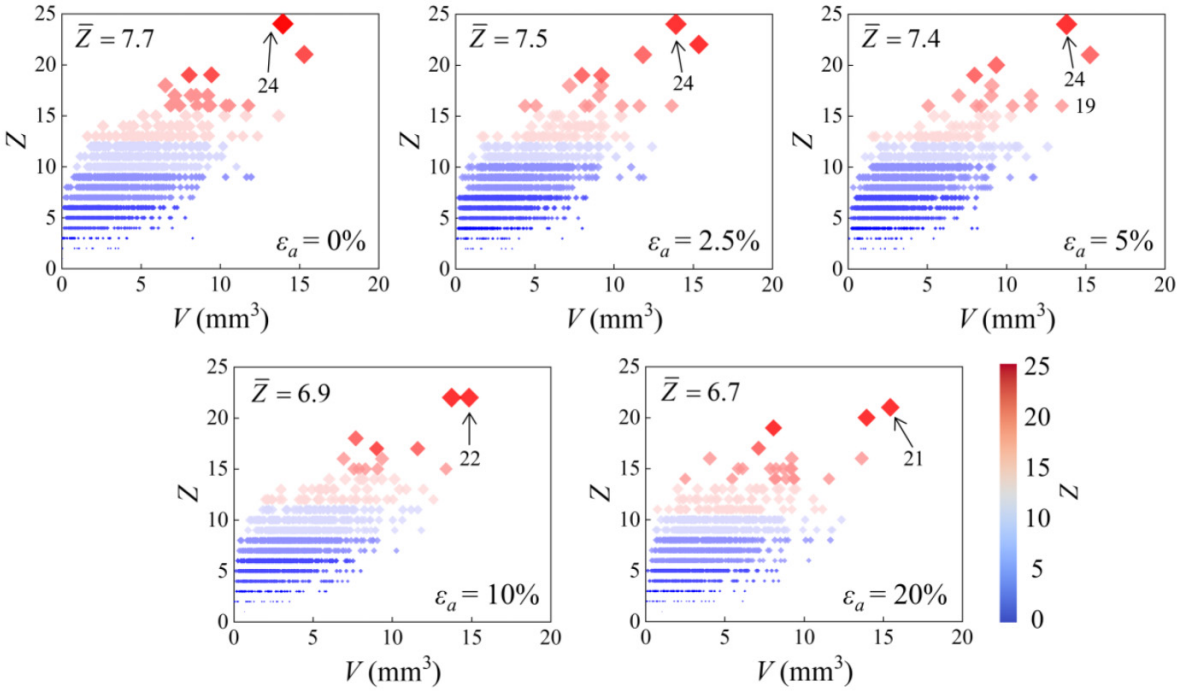

Fig. 12. 3D histograms of contact normal distribution at different axial strains.

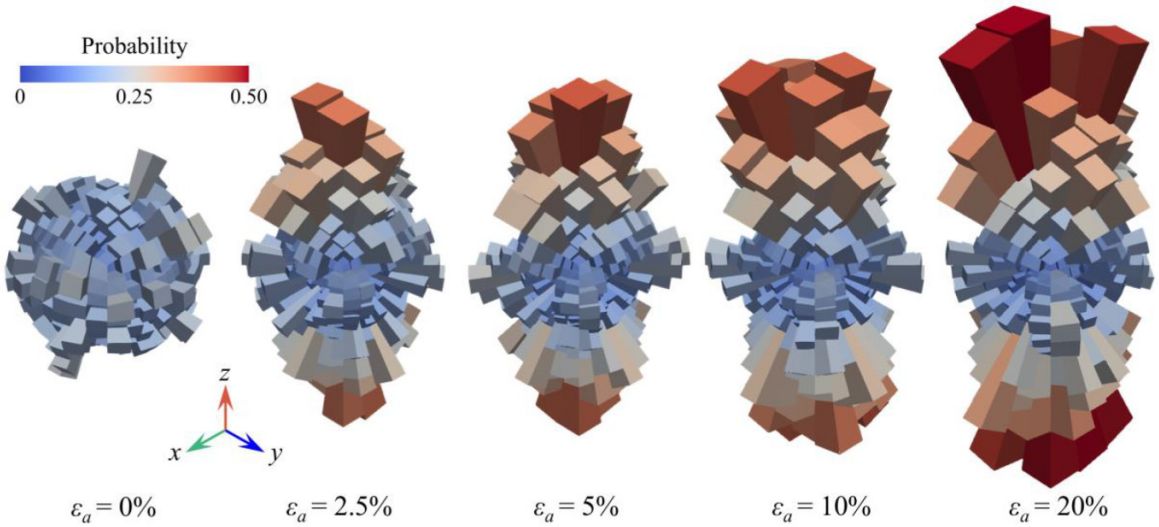

fragmented particles lacking independent reference states, their initial kinematic properties are inherited from their parent particles.

Figure 10 shows a clear 2D representation of granular kinematic features within a representative slice across various axial strain increments. During the early stage of shearing (0%–2.5% axial strain), no significant strain localization of particle displacement or rotation was observed. However, as the axial strain increased from 2.5% to 5%, localized displacement and rotation gradually emerged in the central region of the CSS. Between 5% and 10% axial strain, kinematic localization intensified, characterized by significant particle rearrangements and deformation patterns. These localized deformations directly correspond to macroscopic strain softening and the progressive development of a shear band, consistent with findings from Takano et al. (2015). Finally, at an axial strain increment of 10%–20%, the CSS experienced failure, marked by the formation of a distinct X-shaped shear band. This shear band exhibits a thickness of approximately 6.3 mm (equivalent to 4.5 d_{50}) and an inclination angle of 30°, highlighting its localized nature and structural characteristics. Notably, the shear band is more prominent in the particle rotation pattern, suggesting that particle rotations play a more significant role in strain localization than particle displacements.

Fig. 13. Spatial distribution of particle breakage: (*a*) at 10% and 20% axial strains; and (*b*) classified by breakage modes.

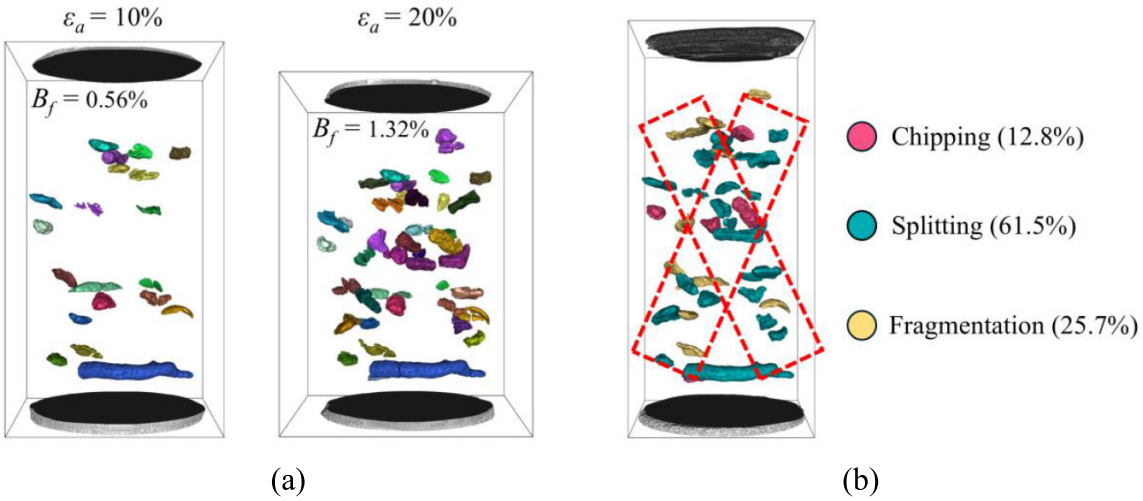

Contact fabric

The coordination number Z, representing the number of contacts per particle, is an important indicator for characterizing the interparticle interactions. Particle contacts are identified by temporarily dilating particle volumes so that contacts between particles can be established (Kong and Fonseca 2019). The orientation of these contacts is defined by the normal vector of the contact area. Note that $\bar{Z}$ denotes the mean coordination number over all particles, defined as follows:

$$\bar{Z} = \frac{2N_c}{N_p} \quad (17)$$

where N_c and N_p denote the number of contacts and particles within the assembly, respectively.

Figure 11 illustrates the relationship between Z and particle volume V at different scans. It is evident that $\bar{Z}$ decreases from 7.7 to 6.7 when axial strain increases from 0% to 20%. This trend aligns with the typical evolution of $\bar{Z}$ for dense granular assembly (Rothenburg and Kruyt 2004). Interestingly, all measurements exhibit a positive correlation, indicating that larger particles tend to have higher Z values and are surrounded by more neighbouring particles. Crucially, maximum coordination values decline from $Z = 24$ at 5% strain to $Z = 21$ at 20% strain. Furthermore, the distribution of large particles (e.g., $V > 10$ mm^3) undergoes significant alteration as axial strain increases from 5% to 20%. These observations suggest that particle breakage may occur between 5% and 20% axial strain.

To investigate the evolution of the contact fabric in the CSS, Fig. 12 presents the 3D histograms of contact normal distribution at different axial strains. Initially, no significant anisotropy is observed after the isotropic stress path. However, as axial strain increases from 0% to 5%, contact normals concentrate along the axial direction. At this stage, axial stress is predominantly transmitted through stable force chains oriented parallel to the compression direction. Afterwards, the shear-induced anisotropy emerges with contact normals reorienting toward directions inclined to the axial direction. This transition reflects the destabilization or even collapse of existing strong force chains if no sufficient contacts are supporting them, consistent with the observation by Oda (1993). Finally, these strong force chains collapse at failure due to the extensive dilatancy, resulting in pronounced anisotropy aligning with the X-shaped shear band shown in Fig. 10*d*.

Particle breakage

Particle breakage failure is one of the most significant characteristics of coral sands (Fukumoto 1992; Coop et al. 2004). It can be classified into three modes (Todisco et al. 2017; Zhao et al. 2020): (1) chipping, where a particle breaks into one slightly smaller particle and several much smaller ones; (2) splitting, where a particle breaks into smaller particles of similar sizes; and (3) fragmentation, where a particle undergoes multiple dramatic failures, resulting in a mass of fragments. To quantify the degree of breakage, the breakage factor B_f (Nakata et al. 1999) is employed, defined as the percentage of particles smaller than the minimum particle size in the intact assembly.

Figure 13*a* illustrates the spatial distribution of particle breakage that occurs within CSS during shear. Breakage failure was first observed at $\varepsilon_a = 10\%$, where 17 particles were crushed into 36 fragments. At the axial strain increased to 20%, breakage continued, resulting in an additional 40 particles fragmenting into 84 pieces. Notably, particle breakage remained relatively limited under the applied effective confining pressure of 100 kPa, evidenced by the B_f value of only 1.32% at $\varepsilon_a = 20\%$. Figure 13*b* depicts the spatial distribution of crushed particles classified by failure modes. Specifically, splitting predominates, accounting for 61.5% of the breakage cases, followed by fragmentation (25.7%) and chipping (12.8%). Interestingly, crushed particles are primarily distributed along the shear band, particularly those resulting from splitting. This phenomenon indicates that particle breakage during shear exhibits distinct anisotropy,

Fig. 14. 3D visualization of particle breakage: (*a*) typical breakage modes; and (*b*) crushed particles and their neighbours.

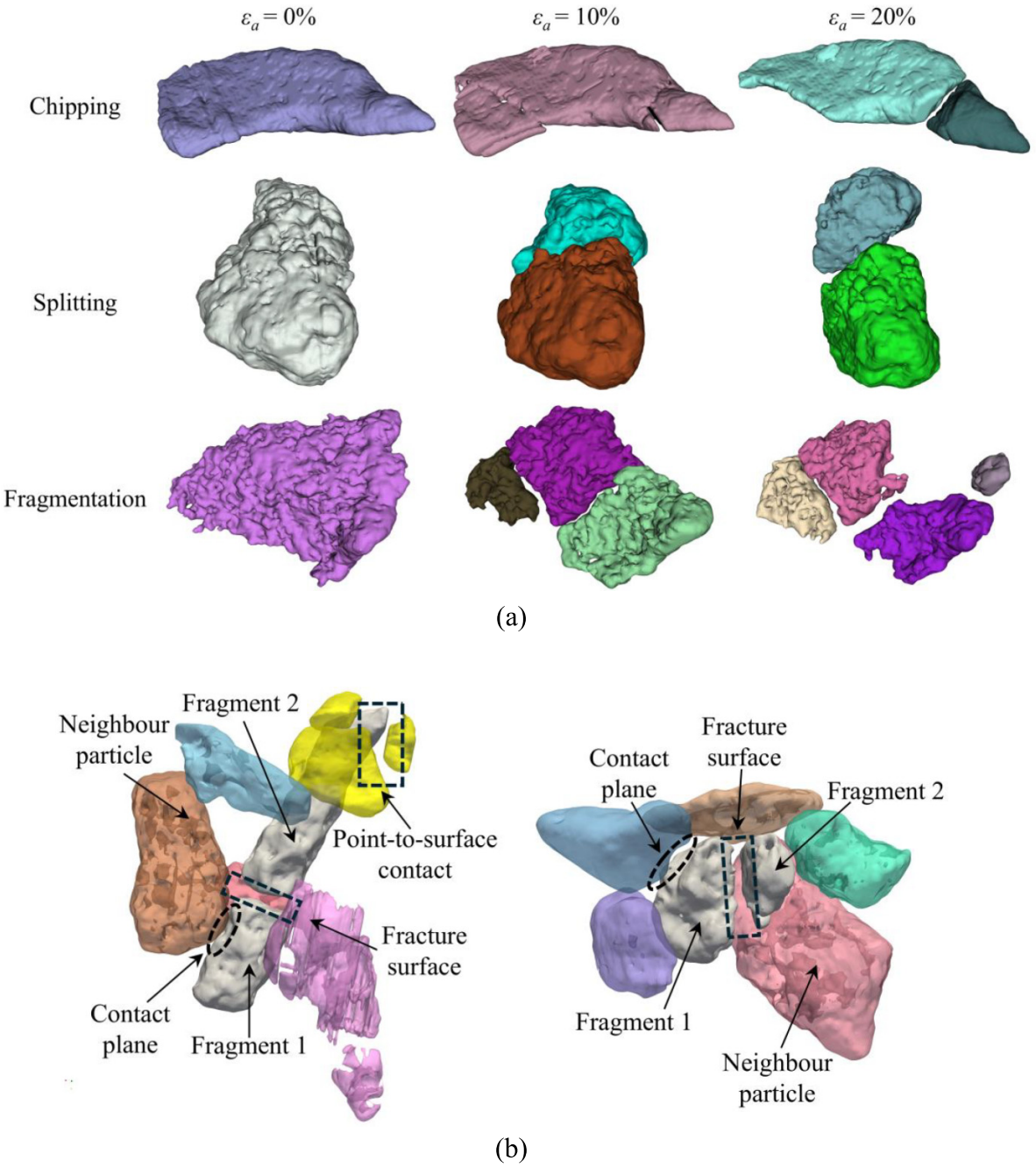

preferentially localizing within zones of intense deformation such as the shear band. The stress anisotropy and localized deformation inherent to shear band development likely contribute to this uneven distribution.

Figure 14*a* presents the representative 3D visualization of three breakage modes. These crushing patterns are similar to the observations provided by Wei et al. (2020). For example, chipping involves localized brittle fracture initiating at particle corners, splitting results in the division of a particle into two major fragments, and fragmentation produces multiple irregular sub-particles. Figure 14*b* shows the neighbor particles around two representative crushed coral sand particles. It can be observed that particle breakage in coral sand is generally induced by stress concentration, as evidenced by straight fracture surfaces. Moreover, at 20% axial strain, crushed particles exhibit a significantly higher mean coordination number ($\bar{Z} = 9.1$) than the assembly-wide average ($\bar{Z} = 6.7$). This demonstrates that particles with more interparticle contacts are more susceptible to crushing under equivalent loading conditions.

Figure 15 classifies crushed particles and their fragments using the Sneed and Folk (1958) shape diagram. Compact and platy morphologies dominate the crushed particle distribution, whereas elongated and bladed forms occur less frequently. Splitting occurs across all shape categories, while chipping and fragmentation primarily affect compact and

Fig. 15. Particle shape classification: (*a*) crushed particles; and (*b*) fragments.

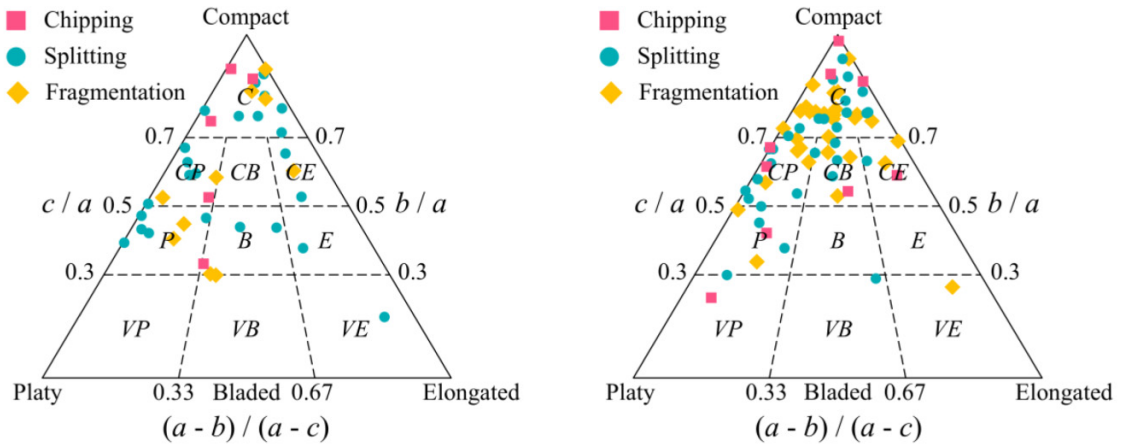

C: Compact; *P*: Platy; *B*: Bladed; *E*: Elongate; *CP*: Compact-Platy; *CB*: Compact-Bladed; *CE*: Compact-Elongate; *VP*: Very Platy; *VB*: Very Bladed; *VE*: Very Elongate; *a*: major dimension; *b*: intermediate dimension; *c*: minor dimension

platy particles. Notably, fragments exhibit stronger clustering within the compact region, indicating greater morphological regularity compared to intact particles. This finding aligns with breakage behaviors reported for quartz and calcite sands by Wu and Wang (2023).

Conclusions

This study establishes a novel framework integrating LVMs for 3D particle reconstruction and OT for 3D particle tracking. The methodology is rigorously validated through in situ mini-triaxial testing of coral sands with μCT, supported by rigorous qualitative and quantitative evaluation. Granular micromechanical analysis revealed fundamental insights into the evolution of soil behavior in coral sands, encompassing particle kinematics, contact fabric, and breakage mechanisms. The main findings of this study are summarised below:

(a) The integration of LVMs with DLO eliminates the need for multi-axis μCT slice processing and provides a generic alternative for accurate 3D particle reconstruction. This framework achieves a twofold increase in computational efficiency while maintaining accuracy comparable to SOTA methods and representing a 60% enhancement over conventional watershed-based approaches.

(b) The OT-based method establishes a new paradigm for 3D particle tracking applicable to coral sands and other granular media. Quantitative results demonstrate its effectiveness in small scan interval (e.g., 2.5% strain) and large scan interval (e.g., 10% strain) tracking, achieving >95% and >70% single-particle accuracy, respectively. End-to-end tracking accuracy of 60% at 20% axial strain confirms its reliability and potential. Notably, the method can also be used to track particle breakage cases during shearing.

(c) Local shearing deformations of coral sands emerge after the stress peak and develop in the strain-softening stage. Larger coral sand particles exhibit more interactions with neighbouring particles and are more susceptible to crushing. Shear-induced anisotropy initially concentrates along the axial direction before the stress peak and gradually reorients to align with the shear band in the softening stage owing to the particle rearrangement.

(d) Slight particle breakage occurs in the coral sand sample under an effective stress of 100 kPa. Splitting is the dominant breakage mode, followed by fragmentation and chipping. The resulting fragments exhibit greater regularity than the original particles. Particle breakage of coral sands is primarily induced by stress concentration and exhibits distinct anisotropy, tending to occur at preferred locations such as the shear band.

Future research will focus on (1) investigating the micromechanical behavior of coral sands through additional μCT-based triaxial tests under diverse loading paths; (2) optimizing the proposed reconstruction and tracking techniques to enhance accuracy and efficiency; and (3) conducting high-fidelity discrete element modeling that incorporates realistic particle shapes and experimentally observed breakage mechanisms.

Acknowledgements

This research was supported by the Research Grants Council (RGC) of Hong Kong Special Administrative Region Government (HKSARG) of China (Grant No.: 15229223, 15227923, 15220221, and E-PolyU501/24) and the National Natural Science Foundation of China (Grant No.: 52408394). The authors thank the BL13HB beamline of the Shanghai Synchrotron Radiation Facility for supporting the in situ mini-triaxial tests on coral sands.

Article information

History dates

Received: 18 August 2025
Accepted: 5 November 2025
Accepted manuscript online: 4 December 2025
Version of record online: 3 February 2026

Copyright

Data availability

All data will be available upon reasonable request.

Author information

Author ORCIDs

Zhen-Yu Yin https://orcid.org/0000-0003-4154-7304

Author notes

Zhen-Yu Yin served as Editorial Board Member at the time of manuscript review and acceptance; peer review and editorial decisions regarding this manuscript were handled by another editorial board member.

Author contributions

Data curation: MW
Methodology: RL
Resources: MW
Software: RL
Supervision: ZY, SH
Validation: ZY
Writing – original draft: RL
Writing – review & editing: SH

Competing interests

The authors declare that they have no competing financial interests or personal relationships that could have appeared to affect the work reported in this paper.

References

Airey, D.W. 1993. Triaxial testing of naturally cemented carbonate soil. Journal of Geotechnical Engineering, **119**: 1379–1398. doi:10.1061/(ASCE)0733-9410(1993)119:9(1379).

Alikarami, R., Andò, E., Gkiousas-Kapnisis, M., Torabi, A., and Viggiani, G. 2015. Strain localisation and grain breakage in sand under shearing at high mean stress: insights from in situ X-ray tomography. Acta Geotechnica, **10**: 15–30. doi:10.1007/s11440-014-0364-6.

Amirrahmat, S., Druckrey, A.M., Alshibli, K.A., and Al-Raoush, R.I. 2019. Micro shear bands: precursor for strain localization in sheared granular materials. Journal of Geotechnical and Geoenvironmental Engineering, **145**: 04018104. doi:10.1061/(ASCE)GT.1943-5606.0001989.

Andò, E., Hall, S.A., Viggiani, G., Desrues, J., and Bésuelle, P. 2012. Grain-scale experimental investigation of localised deformation in sand: a discrete particle tracking approach. Acta Geotechnica, **7**: 1–13. doi:10.1007/s11440-011-0151-6.

ASTM. 2014. Standard test methods for minimum index density and unit weight of soils and calculation of relative density. ASTM international.

ASTM, C. 2006. Standard test method for sieve analysis of fine and coarse aggregates. ASTM C136-06.

ASTM, A.C.D.-18 on. 2017. Standard practice for classification of soils for engineering purposes (unified soil classification system) 1. ASTM international.

ASTM, A.C.D.-18 on. 2015. Standard test method for consolidated drained triaxial compression test for soils. ASTM International.

Chen, R.-C., Dreossi, D., Mancini, L., Menk, R., Rigon, L., Xiao, T.-Q., and Longo, R. 2012. PITRE: software for phase-sensitive X-ray image processing and tomography reconstruction. Journal of Synchrotron Radiation, **19**: 836–845. doi:10.1107/S0909049512029731. PMID: 22898966.

Cheng, Z., and Wang, J. 2018. A particle-tracking method for experimental investigation of kinematics of sand particles under triaxial compression. Powder Technology, **328**: 436–451. doi:10.1016/j.powtec.2017.12.071.

Coop, M.R., Sorensen, K.K., Bodas Freitas, T., and Georgoutsos, G. 2004. Particle breakage during shearing of a carbonate sand. Géotechnique, **54**: 157–163. doi:10.1680/geot.2004.54.3.157.

Davis, J., and Goadrich, M. 2006. The relationship between precision-recall and ROC curves. *In* Proceedings of the 23rd International Conference on Machine Learning—ICML '06. Presented at the the 23rd international conference. ACM Press, Pittsburgh, Pennsylvania. pp. 233–240. doi:10.1145/1143844.1143874.

Desrues, J., Chambon, R., Mokni, M., and Mazerolle, F. 1996. Void ratio evolution inside shear bands in triaxial sand specimens studied by computed tomography. Géotechnique, **46**: 529–546. doi:10.1680/geot.1996.46.3.529.

Dijkstra, J., Gaudin, C., and White, D.J. 2013. Comparison of failure modes below footings on carbonate and silica sands. International Journal of Physical Modelling in Geotechnics, **13**: 1–12. doi:10.1680/ijpmg.12.00004.

Donohue, S., O'sullivan, C., and Long, M. 2009. Particle breakage during cyclic triaxial loading of a carbonate sand. Géotechnique, **59**: 477–482. doi:10.1680/geot.2008.T.003.

Elnur, M., and Alshibli, K.A. 2023. Influence of X-ray beam exposure on the development of gas bubbles during triaxial testing of sand using 3D synchrotron micro-computed tomography. Tomography of Materials and Structures, **3**: 100016. doi:10.1016/j.tmater.2023.100016.

Fan, K., Zheng, Y., Baudet, B.A., and Cheng, Y.P.H. 2021. Investigation of the ultimate particle size distribution of a carbonate sand. Soils and Foundations, **61**: 1708–1717. doi:10.1016/j.sandf.2021.10.002.

Fukumoto, T. 1992. Particle breakage characteristics of granular soils. Soils and Foundations, **32**: 26–40. doi:10.3208/sandf1972.32.26.

Ge, K., Wang, C., Guo, Y.T., Tang, Y.S., Hu, Z.Z., and Chen, H.B. 2024. Fine-tuning vision foundation model for crack segmentation in civil infrastructures. Construction and Building Materials, **431**: 136573. doi:10.1016/j.conbuildmat.2024.136573.

He, S.-H., Ding, Z., Goudarzy, M., Sun, Y., and Yin, Z.-Y. 2024a. Effect of variable confining pressure on the long-term cyclic behaviour of calcareous sand: experimental observation and microstructural interpretation. Canadian Geotechnical Journal, **61**: 311–327. doi:10.1139/cgj-2022-0492.

He, S.-H., Ding, Z., Xia, T.-D., Zhou, W.-H., Gan, X.-L., Chen, Y.-Z., and Xia, F. 2020. Long-term behaviour and degradation of calcareous sand under cyclic loading. Engineering Geology, **276**: 105756. doi:10.1016/j.enggeo.2020.105756.

He, S.-H., Goudarzy, M., Ding, Z., and Sun, Y. 2023. Strength, deformation, and particle breakage behavior of calcareous sand: role of anisotropic consolidation. Journal of Geotechnical and Geoenvironmental Engineering, **149**: 04023002. doi:10.1061/JGGEFK.GTENG-10501.

He, S.-H., Shan, H.-F., Xia, T.-D., Liu, Z.-J., Ding, Z., and Xia, F. 2021. The effect of temperature on the drained shear behavior of calcareous sand. Acta Geotechnica, **16**: 613–633. doi:10.1007/s11440-020-01030-7.

He, S.-H., Yin, Z.-Y., Ding, Z., and Li, R.-D. 2024b. Particle morphology and principal stress direction dependent strength anisotropy through torsional shear testing. Canadian Geotechnical Journal. cgj-2023-0717. doi:10.1139/cgj-2023-0717.

Hu, F., Fang, X., Lei, Y., Yao, Z., Shen, C., and Chen, Z. 2025. Mechanical behavior of coral gravel during triaxial test using X-ray computed tomography. Applied Ocean Research, **154**: 104367. doi:10.1016/j.apor.2024.104367.

Imseeh, W.H., Druckrey, A.M., and Alshibli, K.A. 2018. 3D experimental quantification of fabric and fabric evolution of sheared granular materials using synchrotron micro-computed tomography. Granular Matter, **20**: 24. doi:10.1007/s10035-018-0798-x.

Ji, J.-F., Guo, H., Xue, Y.-L., Chen, R.-C., Fu, Y.-N., Du, G.-H., et al. 2023. The new X-ray imaging and biomedical application beamline BL13HB at SSRF. Nuclear Science and Techniques, **34**: 197. doi:10.1007/s41365-023-01349-2.

Kong, D., and Fonseca, J. 2019. On the kinematics of shelly carbonate sand using X-ray micro tomography. Engineering Geology, **261**: 105268. doi:10.1016/j.enggeo.2019.105268.

Kong, D., and Fonseca, J. 2018. Quantification of the morphology of shelly carbonate sands using 3D images. Géotechnique, **68**: 249–261. doi:10.1680/jgeot.16.P.278.

Li, R., Yin, Z.-Y., and He, S.-H. 2025a. 3D reconstruction of arbitrary granular media utilizing vision foundation model. Applied Soft Computing, **169**: 112599. doi:10.1016/j.asoc.2024.112599.

Li, R., Yin, Z.-Y., He, S.-H., and Sheil, B. 2025b. Enhancement and assessment of large vision models for 3D particle reconstruction from X-ray tomography. Canadian Geotechnical Journal.

Liu, Y., Jin, Y., Azizi, E., and Blumberg, A.J. 2023. CellStitch: 3D cellular anisotropic image segmentation via optimal transport. BioRxiv, 2023–2006.

Lorensen, W.E., and Cline, H.E. 1987. Marching cubes: a high resolution 3D surface construction algorithm. ACM SIGGRAPH Computer Graphics, **21**: 163–169. doi:10.1145/37402.37422.

Mesri, G., and Vardhanabhuti, B. 2009. Compression of granular materials. Canadian Geotechnical Journal, **46**: 369–392. doi:10.1139/T08-123.

Nakata, A.F.L., Hyde, M., Hyodo, H., and Murata. 1999. A probabilistic approach to sand particle crushing in the triaxial test. Géotechnique, **49**: 567–583. doi:10.1680/geot.1999.49.5.567.

Oda, M. 1993. Inherent and induced anisotropy in plasticity theory of granular soils. Mechanics of Materials, **16**: 35–45. doi:10.1016/0167-6636(93)90025-M.

Osco, L.P., Wu, Q., De Lemos, E.L., Gonçalves, W.N., Ramos, A.P.M., Li, J., and Marcato, J. 2023. The segment anything Model (SAM) for remote sensing applications: from zero to one shot. International Journal of Applied Earth Observation and Geoinformation, **124**: 103540. doi:10.1016/j.jag.2023.103540.

Otsu, N. 1979. A threshold selection method from gray-level histograms. IEEE Transactions on Systems, Man, and Cybernetics, **9**: 62–66. doi:10.1109/TSMC.1979.4310076.

Pinzón, G., Andò, E., Desrues, J., and Viggiani, G. 2023. Fabric evolution and strain localisation in inherently anisotropic specimens of anisometric particles (lentils) under triaxial compression. Granular Matter, **25**: 15. doi:10.1007/s10035-022-01305-8.

Ravi, N., Gabeur, V., Hu, Y.-T., Hu, R., Ryali, C., Ma, T., et al. 2024. SAM 2: segment anything in images and videos. doi:10.48550/arXiv.2408.00714.

Rezatofighi, H., Tsoi, N., Gwak, J., Sadeghian, A., Reid, I., and Savarese, S., 2019. Generalized intersection over union: a metric and a loss for bounding box regression. *In* Proceedings of the IEEE/CVF conference on computer vision and pattern recognition. pp. 658–666.

Rothenburg, L., and Kruyt, N.P. 2004. Critical state and evolution of coordination number in simulated granular materials. International Journal of Solids and Structures, **41**: 5763–5774. doi:10.1016/j.ijsolstr.2004.06.001.

Shen, Y., Liu, R., Fan, K., Xu, Q., Lai, Z., and Cheng, Y.P.H. 2024. Microstructure and dynamic behaviours of polyurethane-cured sea sand under traffic–load–induced stress path. Construction and Building Materials, **447**: 138153. doi:10.1016/j.conbuildmat.2024.138153.

Shen, Z., Feydy, J., Liu, P., Curiale, A.H., San Jose Estepar, R., San Jose Estepar, R., and Niethammer, M. 2021. Accurate point cloud registration with robust optimal transport. Advances in Neural Information Processing Systems, **34**: 5373–5389.

Skempton, A.W. 1954. The pore-pressure coefficients *A* and *B*. Géotechnique, **4**: 143–147. doi:10.1680/geot.1954.4.4.143.

Sneed, E.D., and Folk, R.L. 1958. Pebbles in the Lower Colorado River, Texas a study in particle morphogenesis. The Journal of Geology, **66**: 114–150. doi:10.1086/626490.

Takano, D., Lenoir, N., Otani, J., and Hall, S.A. 2015. Localised deformation in a wide-grained sand under triaxial compression revealed by X-ray tomography and digital image correlation. Soils and Foundations, **55**: 906–915. doi:10.1016/j.sandf.2015.06.020.

Todisco, M.C., Wang, W., Coop, M.R., and Senetakis, K. 2017. Multiple contact compression tests on sand particles. Soils and Foundations, **57**: 126–140. doi:10.1016/j.sandf.2017.01.009.

Watanabe, Y., Lenoir, N., Otani, J., and Nakai, T. 2012. Displacement in sand under triaxial compression by tracking soil particles on X-ray CT data. Soils and Foundations, **52**: 312–320. doi:10.1016/j.sandf.2012.02.008.

Wei, H., Zhao, T., Meng, Q., Wang, X., and Zhang, B. 2020. Quantifying the morphology of calcareous sands by dynamic image analysis. International Journal of Geomechanics, **20**: 04020020. doi:10.1061/(ASCE)GM.1943-5622.0001640.

Wiebicke, M., Herle, I., Andò, E., and Viggiani, G. 2021. Measuring the fabric evolution of sand—application and challenges. Geotechnik, **44**: 114–122. doi:10.1002/gete.202000019.

Wu, M., and Wang, J. 2023. Exploring particle breakage in sand under triaxial shearing using combined X-ray tomography and particle tracking method. Géotechnique, 1–40. doi:10.1680/jgeot.22.00351.

Wu, M., and Wang, J. 2019. Registration of point cloud data for matching crushed sand particles. Powder Technology, **347**: 227–242. doi:10.1016/j.powtec.2019.03.001.

Wu, M., Zhou, B., and Wang, J. 2023. On the tracking of shelly carbonate sands using deep learning. Géotechnique, **73**: 974–985. doi:10.1680/jgeot.21.00129.

Yang, H., Shi, J., and Carlone, L. 2021. TEASER: fast and certifiable point Cloud registration. IEEE Transactions on Robotics, **37**: 314–333. doi:10.1109/TRO.2020.3033695.

Yasufuku, N., and Hyde, A.F.L. 1995. Pile end-bearing capacity in crushable sands. Géotechnique, **45**: 663–676. doi:10.1680/geot.1995.45.4.663.

Zeng, K., and Liu, H. 2025. Time-dependent characteristics of coral sand under triaxial stress states. Journal of Geotechnical and Geoenvironmental Engineering, **151**: 04024168. doi:10.1061/JGGEFK.GTENG-12266.

Zeng, K., and Liu, H. 2023a. Experimental study on the time-dependent oedometric compression behavior of calcareous sand. Journal of Geotechnical and Geoenvironmental Engineering, **149**. doi:10.1061/JGGEFK.GTENG-10739.

Zeng, K., and Liu, H. 2023b. Effect of inherent anisotropy on the triaxial compression behavior of coral sand. International Journal of Geomechanics, **23**. doi:10.1061/IJGNAI.GMENG-8003.

Zeng, K., and Liu, H. 2023c. Effect of particle size distributions on the mechanical behavior and particle breakage of coral sands. Granular Matter, **25**: 44. doi:10.1007/s10035-023-01334-x.

Zhang, T., Zhang, C., Song, F., Zou, J., Gao, Y., and Yang, W. 2023. Breakage behavior of silica sands during high-pressure triaxial loading using X-ray microtomography. Acta Geotechnica, **18**: 5195–5211. doi:10.1007/s11440-023-01866-9.

Zhang, Y., Shen, Z., and Jiao, R. 2024. Segment anything model for medical image segmentation: current applications and future directions. Computers in Biology and Medicine, **171**: 108238. doi:10.1016/j.compbiomed.2024.108238. PMID: 38422961.

Zhao, B., Wang, J., Andò, E., Viggiani, G., and Coop, M.R. 2020. Investigation of particle breakage under one-dimensional compression of sand using X-ray microtomography. Canadian Geotechnical Journal, **57**: 754–762. doi:10.1139/cgj-2018-0548.

Zhou, B., Wang, J., and Wang, H. 2018. A novel particle tracking method for granular sands based on spherical harmonic rotational invariants. Géotechnique, **68**: 1116–1123. doi:10.1680/jgeot.17.T.040.

Zhou, Q.-Y., Park, J., and Koltun, V. 2016. Fast Global Registration. *In* Computer Vision—ECCV 2016, Lecture Notes in Computer Science. *Edited by* B. Leibe, J. Matas, N. Sebe and M. Welling. Springer International Publishing, Cham. pp. 766–782. doi:10.1007/978-3-319-46475-6_47.